A multi-scale approach for the stress analysis of polymeric separators in a lithium-ion battery

Xinran Xiao [a,*], Wei Wu [a], Xiaosong Huang [b]

[a] Department of Mechanical Engineering, Michigan State University, 2727 Alliance Dr, Lansing, MI 48910, United States
[b] Chemical Sciences & Materials Systems Lab, General Motors Global Research & Development, 30500 Mound Rd, Warren, MI 48090, United States

ABSTRACT

The separator is a critical component to the durability and safety of a battery. In a Li-ion battery, the dimensional change of the electrodes due to Li insertion/removal and the thermal expansion mismatch between components may induce stresses in the separator. Currently, there is no method to evaluate the stress inside a battery. This paper presents a finite element based multi-scale approach for the stress analysis of the separator in a battery cell. In this approach, the stress and deformation due to Li intercalation in electrode particles and separators is computed with a meso-scale representative volume element (RVE) battery cell sub-model coupled to a 1D macroscopic battery in the multi-physics code COMSOL®. A LiC$_6$/LiPF$_6$/Li$_y$Mn$_2$O$_4$ battery cell is analyzed. As the first step, only the effect of dimensional change due to Li insertion/removal is considered. The simulation results revealed that the stress in the separator vary in phase with the battery cycles. Its state and magnitude depended upon the Young's modulus of the separator, electrode particle size, packing, and the pressure of the cell. The results also suggested that the net cyclic dimensional variation of the battery cell accompanied with Li insertion/removal can be controlled by battery design.

© 2010 Elsevier B.V. All rights reserved.

1. Introduction

To further improve the performance of the separator remains one of the major challenges for large-scale Li-ion batteries used in high energy applications transport [1–3]. The separator is a porous membrane that prevents physical contact between the positive and negative electrodes while enabling ionic transport [1,2]. Three common types of separators are polymeric membranes, nonwoven mats, and ceramic enhanced membranes. Currently, polymeric membranes are used predominantly due to their low cost and relative thinness. A thin separator will facilitate the ionic transport and provide higher energy and power densities [1]. At the same time, it must possess sufficient mechanical properties to withstand the stresses in abuse loading and to resist penetration by fine particles and dendrites. The integrity of the separator is vital to the performance and stability of Li-ion batteries. A short circuit due to poor separator performance can lead to a thermal event resulting in a reduced battery reliability and durability [4,5].

It is well recognized that stress can have a significant impact on the performance of the separator. In a Li-ion battery, in the absence of mechanical loading, two types of non-mechanical stresses can arise. These are the intercalation stress [6–9] and the thermal stress. So far, the investigations on intercalation stresses have been focused on the stresses inside an electrode particle and the fracture of the particle itself [6–12]. Its effects on other components in the battery have not been examined. In literature, the sources of heat generation [13–17] and heat transfer [14,18–23] have been investigated for Li-ion batteries. Nevertheless, there are no published results about thermal stresses.

In a Li-ion battery, the separator is sandwiched between two electrodes. During the charge and discharge cycles, the active particles expand in one electrode and contract in another. At the present time, besides measuring the response of a battery pack in the through thickness direction, there is no method to evaluate the stress in a separator inside a battery with ongoing electrochemical reactions. Furthermore, the stress measured on a battery pack provides an average global stress in the thickness direction. At the local level, the stress state and its amplitude are unknown. The electrodes used in state-of-the-art Li-ion batteries are composites of electrode active particles, conductive particles, binders, and other additives. The surfaces of the electrodes are rough at the microscopic scale. The local stresses may depart significantly from the global stress measured at the surface.

To evaluate the stress in the separator in a battery, the deformation of both electrodes and their interactions must be considered. For this purpose, a multi-scale model for a Li-ion battery cell with

* Corresponding author. Tel.: +1 517 884 1606; fax: +1 517 884 1601.
E-mail addresses: xinran@msu.edu, xinran@egr.msu.edu (X. Xiao).

the inclusion of the multi-physics related to the two types of non-mechanical stresses and the battery electrochemical kinetics is under development. To begin with, a multi-scale model is developed for a $LiC_6/LiPF_6/Li_yMn_2O_4$ battery cell based on an existing 1D Li-ion battery model in COMSOL® [24]. This strategy eliminates the effort of building a new battery model and allows us to focus on the task of stress analysis.

The work on a prototype 2D multi-scale model with the inclusion of intercalation stress has been completed. This paper presents the modeling approach for the multi-scale model and the results of preliminary numerical investigations using the 2D model. The extension of the model with heat generation and thermal stress is still ongoing [25] and will be presented separately.

2. Previous work on the analysis of intercalation stress

Intercalation stress involves multi-physics. In the published literature, the analysis of intercalation stress has been carried out for a single electrode particle using a variety of techniques. Christensen and Newman [7,8] considered the intercalation stress inside a spherical particle with electrochemical reactions. For a spherical shaped particle, the problem was reduced to one dimensional (1D) and described by a set of 20 equations. These coupled equations were solved by using a finite difference method. Another solution method is a multi-scale approach. In this approach, the differential equations of the multi-physics problem are divided into two sets. The first set consists of the equations associated with the electrochemical kinetics of the battery. The second set consists of the diffusion equation and constitutive equations between stress and strain. This approach allows different physical phenomena to be represented by models at different scales. Golmon et al. [26] developed a multi-scale model that considers the electrochemical–mechanical interaction when embedding batteries into a structural composite. In the model, the battery kinetics was analyzed by a 1D battery model based on that of Doyle et al. [27,28]. The Li+ flux from the 1D model was mapped to a 3D model of a particle in a deformable matrix according to its depth in the electrode. The stresses in the composite electrode were then evaluated using a micromechanics model [29] based on the Mori–Tanaka (M–T) effective-field theory [30].

Alternatively, the analysis of intercalation stresses in particles can be conducted by applying a prescribed Li+ flux at the particle boundary without a battery model [6,9,11,31]. Zhang et al. [9] investigated the intercalation stress for a single active particle using a detailed 3D finite element (FE) model with this approach. Cheng and Verbrugge provided a 1D analytical solution for intercalation stresses in nano-sized particles with the consideration of surface tension and surface modulus [6]. The analytical solution has been extended to consider the cyclic stress inside the particle under a predefined periodic potential boundary condition [31].

2D and 3D battery models have also been developed [12,32]. Garcia et al. [12] developed a 2D battery model for a $LiC_6/Li_yMn_2O_4$ cell and implemented it in the Object Oriented Finite (OOF) Element program. The model considered the intercalation stress in the composite cathode consisting of $Li_yMn_2O_4$ particles in the matrix of an electrolyte. The electrolyte was assumed to be a compliant gel with negligible resistance to deformation. With a low volume fraction of active particles in the model, this treatment limited the effect of intercalation stress to individual particles. Wang and Sastry [32] developed a 3D meso-scale battery model for the prediction of the electrochemical performance of the Li-ion battery utilizing the Nernst–Planck equation in COMSOL®, a multi-physics FE package. The stress was not included in the meso-scale model.
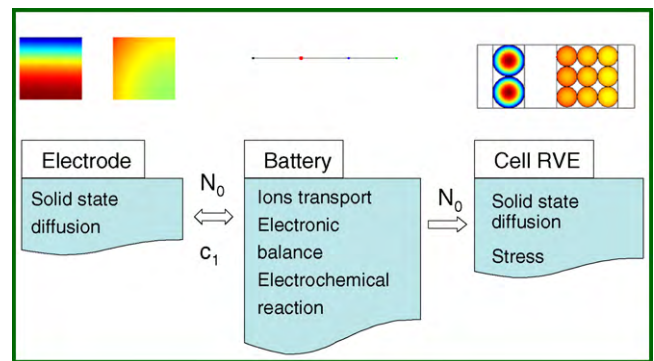

Fig. 1. Schematic of the multi-scale model showing the physical phenomena considered in each sub-model and their coupling relationships.

3. A multi-scale model for a battery cell

A major difficulty in modeling the stress due to Li intercalation at the battery cell level is the multi-scale, multi-physics nature of the problem. A separator is sandwiched between two electrodes. In the thickness direction, a basic cell ranges between 150 and 300 μm. The intercalation stress occurs at the level of individual active particles which have an average size of 5–20 μm. On the other hand, in a planer (pouch) cells used in large-scale battery, the in-plane dimension of a single cell is in the range of 20–30 cm. The aspect ratio for a single planer cell is at the order of 10^3.

To overcome the difficulty of the large aspect ratio of a planer cell, a representative volume element (RVE) approach was employed together with a multi-scale approach. RVE by definition is the smallest material volume element of a heterogeneous material for which the effective constitutive representation is a sufficiently accurate model to represent the mean constitutive response of the material [33]. In this work, the concept of RVE is applied in a slightly different sense. RVE is the smallest volume of a battery cell that represents the mechanical and physical response at the center region of a planar cell. Ideally, a RVE model should be sufficient to reveal the response of individual components in a battery.

Fig. 1 presents the schematics of the multi-scale model and the physics considered at each scale. In this model, the equations of the multi-physics problem were divided into three sets and solved by three sub-models at three different scales. The battery electrochemical kinetics was solved by a 1D macroscopic battery model based on that of Doyle et al. [27,28]. The Li diffusion in the active particles and the interaction between the particle diffusion and battery kinetics were solved using a microscopic sub-model for spherical particles in the electrode. The stress analysis was carried out at the level of a basic battery cell using a RVE. Compared to the other two sub-models, the RVE sub-model is at a meso-scale. It allows the investigation of mechanical responses of individual components in a battery environment.

The sub-models for the first two scales have been reported in literature and available in COMSOL® [24] for a $LiC_6/LiPF_6/Li_yMn_2O_4$ battery cell. The current three-scale model is built upon the battery model in COMSOL. For the sake of completeness, a brief description of the first two sub-models and their coupling are provided in the following text, in addition to the discussion of RVE sub-model.

3.1. Battery sub-model

An 1D battery model has been developed by Doyle et al. [27,28]. The model considers an electrochemical system consisting of a negative electrode, a separator, and a positive electrode. The electrodes and separator are porous and saturated with a liquid electrolyte. The porous solid together with the electrolyte is modeled as a

homogenized composite medium. The volume fraction of the electrolyte equals the porosity. The contribution of the electrolyte phase in Li+ transport is considered by introducing a porosity parameter in the governing equation, as to be discussed in this section. The Li transport in active particles is considered by a separated model to be discussed in Section 3.2.

In the COMSOL 1D battery model, the solid phase is denoted as phase 1 and the electrolyte phase is denoted as phase 2. The variables and parameters that appear in both phases are distinguished by a subscript 1 or 2.

In the electrolyte phase (phase 2), Li+ is transported through two mechanisms: diffusion and migration. Considering a small volume in electrolyte, the governing equation for material conservation is obtained as

$$\varepsilon \frac{dc_2}{dt} = \nabla \cdot (D_2^{eff} \nabla c_2) - \frac{1}{F} \mathbf{i}_2 \cdot \nabla t_+ + S_a j_n (1 - t_+) \tag{1}$$

where c_2 is the Li+ concentration, D_2^{eff} is the effective diffusivity, ε is the porosity (volume fraction of the electrolyte), F is the Faraday's constant, $\mathbf{i}_2$ is the current density in the electrolyte, t_+ is the transport number representing the percentage of the current in the electrolyte carried by Li+, S_a is the specific surface area of the electrode, and j_n is the charge transfer current density at the interface and

$$\nabla \cdot \mathbf{i}_2 - F S_a j_n = 0 \tag{2}$$

Eq. (1) states that the change in Li+ concentration is the net result of Li+ diffusion (1st term), Li+ migration in an electrical field (2nd term), and the concentration change induced by the Li+ that leaves or enters the electrolyte through the interface with the active particles (3rd term). The 3rd term vanishes for a volume that is not adjacent to an active particle.

For ionic charge balance, the governing equation is given as

$$\nabla \cdot \left(-k_2^{eff} \nabla \phi_2 + \frac{2RTk_2^{eff}}{F} \left(1 + \frac{\partial \ln f}{\partial \ln c_2} \right) (1 - t_+) \nabla (\ln c_2) \right) = S_a j_n \tag{3}$$

Here R denotes the gas constant, T denotes the temperature, k_2^{eff} is the effective ionic conductivity, ϕ_2 is the ionic potential, and f is the ionic activity coefficient. Eq. (3) is derived for an electrolyte of a binary salt. It can be considered as a modified Ohm's law. The 1st term in the bracket is equivalent to that for a solid conductor. The 2nd term accounts for the effect of Li+ ion concentration on the ionic current [26].

In the solid phase of the composite electrode, the charge balance obeys Ohm's law:

$$\nabla \cdot (-k_1 \nabla \phi_1) = \mathbf{i}_1 \tag{4}$$

where ϕ_1 is the electronic potential of the solid phase and k_1 denotes the electronic conductivity. $\mathbf{i}_1$ is the current density in the solid phase and

$$\nabla \cdot \mathbf{i}_1 + F S_a j_n = 0 \tag{5}$$

3.2. Electrode sub-model

At the surface of the active particle, Li+ becomes Li through a reduction reaction. In the active particles, Li moves through diffusion. For a spherical particle, the diffusion equation reduces to 1D with the spherical coordinate:

$$\frac{dc_1}{dt} + \frac{1}{r^2} \frac{\partial}{\partial r} \left(-r^2 D_1 \frac{\partial c_1}{\partial r} \right) = 0 \tag{6}$$

3.3. Coupling between the battery and electrode sub-models

The Li+ flux N_0 at the particle boundary in the electrode sub-model is related to the local current density in the electrolyte phase in the battery sub-model through

$$N_0 = \frac{-j_n}{F} \tag{7}$$

The amplitude of j_n is determined by the interface reaction kinetics with the Butler–Volmer expression:

$$j_n = i_0 \left\{ \exp\left(\frac{\eta F}{RT} \right) - \exp\left(\frac{(-\eta)F}{RT} \right) \right\} \tag{8}$$

where η is the local surface overpotential, which is defined as

$$\eta = \phi_1 - \phi_2 - E_{ref}(c_{1,surf}) \tag{9}$$

and i_0 denotes the exchange current density and is determined by

$$i_0 = k_0 \sqrt{c_2(c_{1,max} - c_{1,surf})c_{1,surf}} \tag{10}$$

In Eqs. (9) and (10), E_{ref} is the electrode particle's equilibrium potential, k_0 is the reaction rate constant, $c_{1,surf}$ is the Li concentration at the surface of the particle, and $c_{1,max}$ is the maximum achievable Li concentration in the particle.

3.4. RVE model

To carry out stress analysis at the level of a battery cell, a RVE sub-model was added to the existing battery and electrode sub-models, as illustrated in Fig. 2. The RVE sub-model presented in Fig. 2c is a prototype quarter-sized 2D model.

The multi-physics phenomena considered in the RVE sub-model include the diffusion of Li inside the electrode particles and the stress due to Li intercalation as well as mechanical loading. To reduce the modeling effort and allow active particles of different sizes and shapes to be considered, the diffusion process in the RVE sub-model had one-way coupling with the 1D battery sub-model. In this way, even if the volume fraction of the active particles of a certain shape and packing pattern cannot be realized accurately in the RVE sub-model, it would not affect the battery kinetics in the 1D battery sub-model.

The Li+ flux N_0 computed in the 1D battery sub-model was mapped to individual particles in the RVE by direct projection. The N_0 in the RVE model, therefore, varies only in the through thickness direction as in the 1D battery.

For an isotropic material, the constitutive relationship for the strain ε^{me} due to the mechanical stress is given as [34]:

$$\varepsilon_{ij}^{me} = \frac{1}{E}((1 + \nu)\sigma_{ij} - \nu\sigma_{kk}\delta_{ij}) \tag{11}$$

where σ_{ij} represents the stress components, E is Young's modulus, ν is Poisson's ratio of the material, and δ_{ij} is the Dirac delta function. In this work, E and ν were treated as constants. The variation of the elastic constants with temperature and Li concentration was not considered.

The total strain is the summation of the mechanical strain and two types of eigenstrains such that

$$\varepsilon_{ij} = \varepsilon_{ij}^{me} + \varepsilon_{ij}^{ei\_T} + \varepsilon_{ij}^{ei\_c} \tag{12}$$

It should be noted that, during charge–discharge cycling, chemical reactions such as electrode decomposition and electrolyte reduction may generate gas [35] which in turn will cause a gradual increase in the volume of a Li-ion battery. This gradual degradation phenomenon is not considered in this work.

The temperature variation induced eigenstrain ε^{ei_T} in an isotropic material is given by [34]

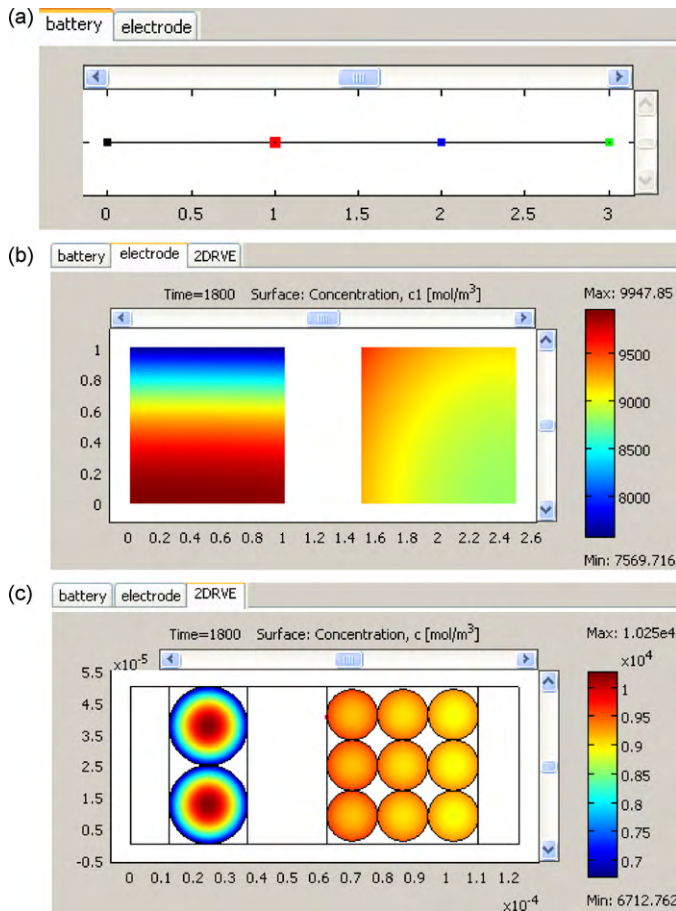$$\varepsilon_{ij}^{ei\_T} = \alpha_{ij} \, \Delta T \, \delta_{ij} \tag{13}$$

Fig. 2. Illustration of the multi-scale modeling approach. The electrochemical performance of the battery is evaluated with an existing 1D Li-ion battery model in COMSOL® which consists of two sub-models: (a) battery and (b) electrode. The stress analysis for the components in a cell is performed concurrently using (c) a meso-scale RVE sub-model.

where ΔT is the temperature variation and α_{ij} is the coefficient of thermal expansion.

The diffusion induced eigenstrain ε^{ei_c} in an isotropic material is considered through a diffusion/thermal analogy such that [6,36]:

$$\varepsilon_{ij}^{ei\_c} = \frac{1}{3} \Delta c \, \Omega \delta_{ij} \tag{14}$$

where Δc is the change in the concentration of the diffusion species and Ω is the partial molar volume of the solute in the host material.

The partial molar volume can be calculated using the following equation [9]:

$$\Omega = \frac{3\varepsilon}{\Delta y \, C_{max}} \tag{15}$$

where ε is the strain caused by intercalation expansion along the major axis of the material, Δy refers to the change in the number of lithium atoms that occurs during the charge and discharge cycles, and C_{max} is the stoichiometric maximum concentration.

The FE model of the RVE sub-model is in the Cartesian coordinate. The diffusion equation for an isotropic solid in the Cartesian coordinate is given by

$$\frac{\partial c}{\partial t} = D(\nabla^2 c) \tag{16}$$

In the RVE sub-model, the diffusion equation was solved for the active particles in both electrodes. The stress analysis included all phases. In the current model, stress enhance diffusion [7–9] was neglected.

4. Modeling details

4.1. FE representation for 2D RVE

To begin with, prototype quarter-sized and half-sized 2D RVE sub-models were built for the 1D battery $LiC_6/LiPF_6/Li_yMn_2O_4$ battery in COMSOL® [24]. Fig. 2c presents a quarter-sized 2D RVE sub-model. From left to right, the components included were current collector, negative electrode, separator, positive electrode, and current collector. Their respective through thickness dimensions (horizontal axis) were 12.5/25/25/48/12.5 μm. In its thickness direction, the electrode in the quarter-sized sub-model had a dimension that was equivalent to a quarter of the electrode in the 1D battery model in COMSOL® [24]. The thickness of the separator was about a half of that of the 1D battery model. The active particles in the 1D battery model in COMSOL® [24] had a radius of 12.5 μm in the negative electrode and a radius of 8 μm in the positive electrode. Keeping the same particle size, the resulted quarter-sized RVE sub-model had one layer of particles in the negative electrode and three layers of particles in the positive electrode. The construction of the half-sized RVE followed the same rule.

In the multi-scale model, some of the parameters in the 1D battery sub-models need to be modified with the change in battery dimension. Table 1 presents the key parameters of the original 1D battery model in COMSOL® [24] with those in the multi-scale model with a quarter-sized and a half-sized 2D RVE sub-model. All other parameters in the multi-scale model were kept the same as in the original 1D battery model unless otherwise specified in the following text.

The FE mesh for the quarter-sized 2D RVE sub-model and the boundary conditions for stress analysis were shown in Fig. 3. The
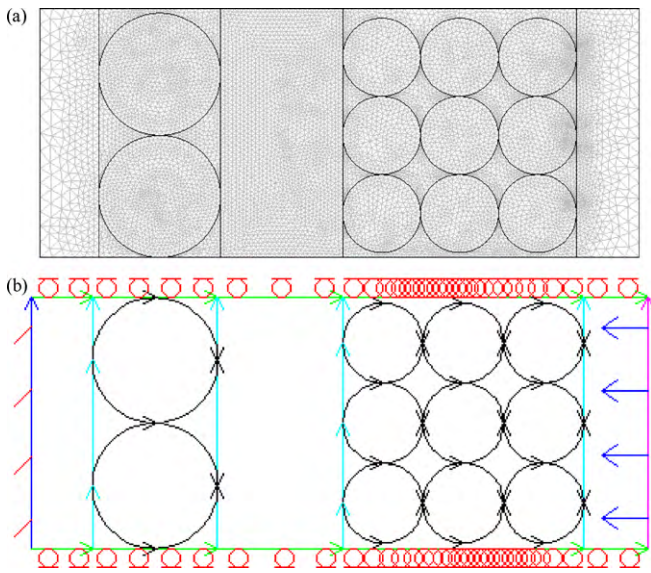
Table 1
Parameters in the COMSOL® 1D battery model [24] and in the multi-scale model with a quarter-sized or a half-sized 2D RVE.

Parameter	Unit	1D battery model in Comsol [24]	The RVE in multi-scale model[a]	
			Quarter-sized	Half-sized
Li_yC_6 negative particle radius	μm	12.5	12.5	12.5
$Li_yMn_2O_4$ positive particle radius	μm	8	8	8
Negative electrode thickness	μm	100	25	50
Positive electrode thickness	μm	183	48	96
Separator thickness	μm	56	25	25
SOC in Li_yC_6 Discharged		0.271	0.227	0.227
SOC in Li_yC_6 Charged		0.563	0.611	0.611
SOC in $Li_yMn_2O_4$ Discharged		0.472	0.569	0.569
SOC in $Li_yMn_2O_4$ Charged		0.170	0.231	0.231

[a] All other parameters in the multi-scale model were kept the same as those in the original 1D battery model in Ref. [24].

(a)

(b)

Fig. 3. (a) The FE mesh for the quarter-sized 2D RVE sub-model and (b) the boundary conditions for stress analysis. A periodical boundary is assigned for the in-plane direction (lower and upper boundaries). A fixed-free (with pressure) boundary condition is assumed for the thickness direction. The left hand side is fixed while the right hand side is subjected to pressure normal to the boundary. Case studies were performed with a pressure of 10 or 50 psi.

analysis was carried out assuming a plane strain condition. The displacement field across different components was assumed to be continuous and modeled with a continuous mesh. It should be noted that in a battery, the active particles are in contact with, instead of bonded to, the separator. The relative movement between the separator and electrodes may happen at a local area at microscopic level. To take into consideration of this effect requires a contact definition between the particles and separator. It was possible to establish a contact relationship between the particles and separator in a stand alone model. When incorporating the RVE sub-models with contact definition in the multi-scale model, convergence problems arise. The problem became worsen when a compliant electrolyte phase was added. A continuous mesh, therefore, was adopted in the RVE sub-models in the paper.

A periodical boundary was assigned at the lower and upper boundaries, i.e. in the in-plane direction. A fixed-free (with pressure) boundary condition was prescribed in the through thickness direction where the left end was fixed while the right end was subjected to a pressure normal to the boundary. The pressure levels investigated in this work were 10 and 50 psi.

The diffusion analysis was performed for active particles only. The Li+ flux computed by Eq. (7) according to the local current density was mapped to the surface of the particles with a multiplier factor of 1.5. This correction factor was introduced to account for the difference in the surface area/volume ratio for active particles between the sub-models. The 1D battery and electrode sub-models were formulated for spherical shaped particles based on spherical symmetry. In the 2D RVE sub-models, the active particles were represented by circles. A circle in 2D actually represents a cylindrical shape rather than a spherical particle in 3D. The surface area/volume ratio is $3/R$ and $2/R$ for a sphere and a cylindrical shape with a radius of R, respectively. In other words, for the same value of flux, a spherical shape will receive 1.5 times of Li+ per volume as compared to a cylindrical shape of the same radius. To achieve the same distribution of Li concentration in the active particles in 2D RVE sub-model, a multiplier of 1.5 to the flux from the 1D battery sub-model is needed. With this correction, similar Li concentration

Table 2
Material constants of the $Li_yMn_2O_4$ particles.

Property	Unit	Value	Comment
Young's modulus, E	GPa	10	[9]
Poisson's ratio, ν		0.3	[9]
Density, ρ	kg m^{-3}	4140	[28]
Diffusion coefficient, D	m^2 s^{-1}	7.08×10^{-15}	[9]
Partial molar volume, Ω	m^3 mol^{-1}	3.5×10^{-6}	[9]
Stoichiometric maximum concentration, C_{max}	mol m^{-3}	2.29×10^4	[28]
Isotropic volume expansion SOC = 0.2–0.995		6.5%	[9]

profiles were obtained in the electrode and 2D RVE sub-models, as shown in Fig. 2b and c.

The active particles had an initial condition of a uniform Li concentration. The equilibrium concentrations for particles in the two electrodes in charged or discharged states are provided in terms of the state of charge (SOC) in Table 1. The initial stress in the particles with a uniform Li concentration was assumed to be zero.

4.2. Material modeling

4.2.1. Active particles

The active particles in the two electrodes were modeled with an elastic material law. In this paper, the elastic properties of the active particles were assumed to be constant. It has been shown that the elastic modulus of the active particles may be a function of SOC. Using first principles density function theory, Qi et al. [37] computed the lattice parameters and elastic properties of several intermediate structures of Li in graphite and found that the Young's modulus can increase up to three-fold. The effect of a SOC dependent elastic modulus has been evaluated for a single graphite particle [38].

Tables 2 and 3 provide the material constants used in computing the intercalation stress for $Li_yMn_2O_4$ particles in the positive electrode and Li_yC_6 particles in the negative electrodes, respectively. The calculation of intercalation stress in $Li_yMn_2O_4$ has been well established [6–9]. The material constants in Table 2 were obtained from literature. The calculation of intercalation stress in Li_yC_6 particle has not been reported previously. The elastic modulus and the partial molar volume for Li_yC_6 in Table 3 were estimated values.

The elastic modulus of Li_yC_6 calculated in theoretical studies is in the range of 28–108 GPa [37,39]. These values are high as compared with those reported in the data sheet of graphite par-

Table 3
Material constants of the Li_yC_6 particles.

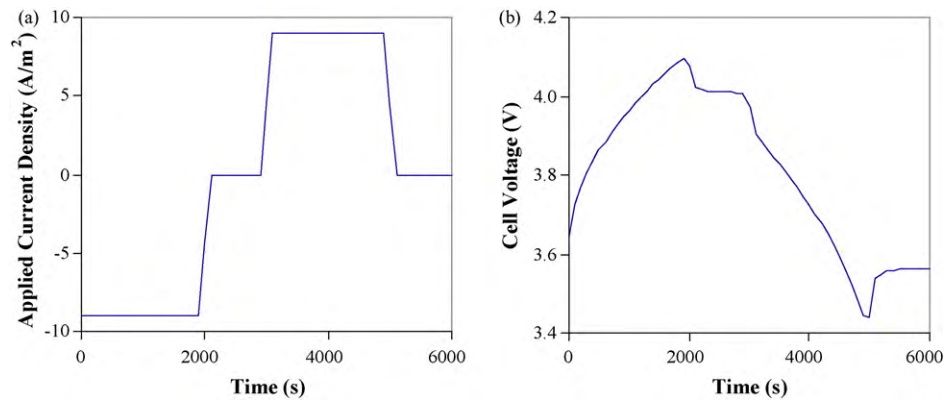| Property	Unit	Value	Comment
Young's modulus, E	GPa	12	Estimated value
Poisson's ratio, ν		0.3	Estimated value
Density, ρ	kg m^{-3}	1900	[28]
Diffusion coefficient, D	m^2 s^{-1}	3.9×10^{-14}	[28]
Partial molar volume, Ω	m^3 mol^{-1}	4.17×10^{-6}	Calculated with Eq. (15)
Stoichiometric maximum concentration, C_{max}	mol m^{-3}	2.64×10^4	[28]
		3.06×10^4	[41]
Isotropic volume expansion SOC = 0–1.0		11%	Estimated value

Fig. 4. (a) A battery cycle for a half-sized unit cell at a 1.03C (i = 9 A m^{-2}) charge and discharge rate. The cycle consists of charge (0–2000 s), open circuit period (2000–3000 s), discharge (3000–5000 s), and open circuit period (5000–6000 s). (b) The cell voltage (ϕ_1) histories obtained by simulations.

ticles, which are in the range of 9–15 GPa [40]. This discrepancy is due to the imperfection and porosity in commercial grade graphite particles. The present work concerned a battery with commercially available graphite particles. A value of 12 GPa was therefore selected.

The partial molar volume for Li$_y$C$_6$ was calculated using Eq. (15). The stoichiometric maximum concentration C_{max} for Li$_y$C$_6$ was given as 2.64×10^4 mol m^{-3} in [24,28] and 3.06×10^4 mol m^{-3} in [41]. From C to LiC$_6$, $\Delta y = 1$. Assuming a maximum volume change of 11% and a $C_{max} = 2.64 \times 10^4$ mol m^{-3}, the partial molar volume for Li$_y$C$_6$ was estimated as

$$\Omega = \frac{3\varepsilon}{\Delta y\, C_{max}} \approx \frac{3 \times (0.11)^{1/3}}{1 \times 2.64 \times 10^4} = 4.17 \times 10^{-6}\ \text{m}^3\ \text{mol}^{-1}$$

4.2.2. Separator

Separators are porous membranes. A polymeric separator may have anisotropic properties. In this preliminary investigation, the separator was considered as a homogeneous material and modeled with an isotropic elastic material law. Simulations were conducted with a set of assumed materials constants, as listed in Table 4. A majority of the investigations were carried out with two levels of Young's modulus, E = 50 MPa, representing a typical PVDF separator, and E = 200 MPa, representing a typical polyolefin separator.

Table 4
Assumed material constants for the separator.

Property	Unit	Value	Comment
Young's modulus (polyolefin), E	MPa	200	Estimated value
Young's modulus (PVDF), E	MPa	50	Estimated value
Poisson's ratio, ν		0.35	Estimated value
Density, ρ	kg m^{-3}	900	Estimated value

4.2.3. Others

The electrolyte phase in the electrodes was represented using a viscoelastic material model with an instantaneous shear modulus of 0.2 MPa. This value is about an order higher than that reported for compliant gels [42]. A very low modulus, however, tends to lead to a convergence problem. The assumed value of 0.2 MPa was more than two orders lower than the modulus of the separator and, therefore, was judged as acceptable.

The current collector was assumed to be copper and represented with an elastic material law.

4.3. Numerical experiments

Numerical experiments were conducted with a charge–discharge cycle with an input current density equivalent to a charge rate of 1C. The cycle consists of a charge (0–2000 s), open circuit (2000–3000 s), discharge (3000–5000 s), and another open circuit period (5000–6000 s). Fig. 4a plots the current density
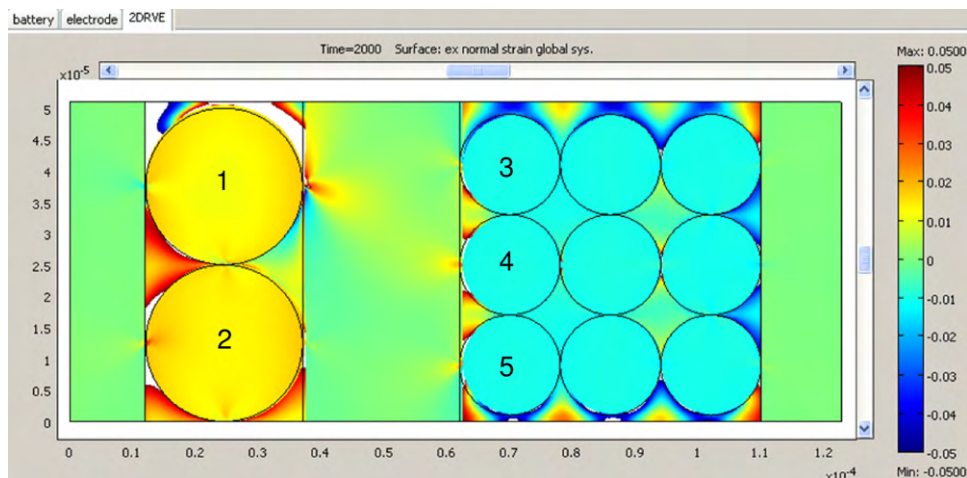

Fig. 5. The predicted through thickness strain distribution at the end of discharge (2000 s) under a fixed-free (10 psi) boundary condition using a quarter-sized 2D RVE model. The areas with a void like appearance have a strain value beyond the range and hence are removed from the display. Particles 2 and 4 have a close-packed pattern whereas particles 1, 3 and 5 have a loose-packed pattern. The maximum strain in the separator is found near a loose-packed particle of larger diameter.

history for a 1C charge–discharge cycle for a half-sized cell. The history of cell voltage (the voltage of the solid phase ϕ_1) obtained by simulations using the 1D battery sub-model is presented in Fig. 4b.

5. Numerical investigations

5.1. The effect of particle packing

The initial numerical investigations were conducted with a prototype quarter-sized RVE sub-model. The particles in this RVE had two packing patterns. As shown in Fig. 5, particles 2 and 4 are in contact with its neighbors. This packing pattern is referred as a close-packed pattern thereafter. On the other hand, particles 1, 3 and 5 are separated with its neighbors by a space filled with electrolyte, which is referred as a loose-packed pattern in the following text.

Numerical simulations revealed that the stress and strain fields in the separator were not uniform and varied in-phase with the charge–discharge cycle. For the charge–discharge cycle studied in this work, a stress and strain maxima occurred at the end of the charge period ($t = 2000$ s) at the surface in contact with the negative particles. At the side in contact with the positive particles, it happened at the end of discharge ($t = 5000$ s). When other conditions were equal, the maximum strains and stresses were found near particles with a larger diameter.

Fig. 5 displays the distribution of x-strain component at $t = 2000$ s. In the RVE model, the strain in the electrolyte phase was much higher as compared to that in other components. To ease the analysis of strain in the separator, in Fig. 5, the range of the display scale is set to ± 0.05 and therefore, the areas with a higher strain have a void like appearance.

Fig. 5 reveals that the strain in the separator is higher in the area adjacent to a particle with a loose-packed pattern. This is evident by comparing the strain distribution in the vicinity of particle 1 with that of particle 2. The same trend was observed for y-strain component. It was suspected that this high stress might be due to the limitation of the prototype RVE model that a continuous mesh is employed, instead of a contact definition, between the particles and the separator.

FE models with a continuous mesh between components may be employed to study the stress behavior of a RVE with close-packed particles. With a sufficient number of particles, the central area of the RVE may reveal information about the stress and strain history in a battery cell. For this purpose, half-sized 2D RVE models were investigated. The final RVE model consisted of a total 88 particles, which had 16 negative particles and 72 positive particles. Further investigations were carried out with this RVE.

5.2. Thickness variation

The dimensional change in the thickness direction of the battery is a measurable parameter. To validate the model, the displacement in the thickness direction was investigated.

It was observed, upon applying a surface pressure, there was an immediate reduction in the cell thickness. This dimensional change was absorbed by the deformation of the separator. The amount of deformation depended upon the elastic modulus of the separator and the pressure at the surface of the cell. Fig. 6 presents the displacement field of the RVE at $t = 0$ s. The simulation was conducted with a separator of $E = 50$ MPa under a pressures of 10 psi. At $t = 0$ s, the volume of the active particles remained the same. The deformation was, therefore, entirely due to the pressure. As seen in Fig. 6, at the microscopic level, the deformation was not uniform in the separator. The areas in contact with the particles exhibited a larger deformation. Further evidence is provided by the displacement profiles obtained at the surfaces of the separator, as displayed
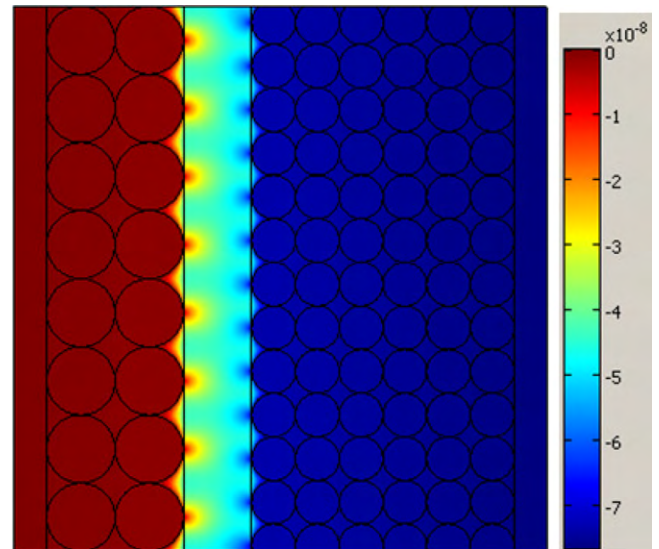

Fig. 6. The through thickness displacement field at $t = 0$ s predicted by a half-sized 2D RVE with close-packed particles. The RVE had a separator with a Young's modulus of $E = 50$ MPa under a fixed-free (10 psi) boundary condition.

in Fig. 7. It clearly shows the indentation of particles into the separator. The indentation appeared to increase with increasing in the size of the particle and decreasing in the Young's modulus of the separator.

The local indentation of particles at the surface of the separator has further implications. The particles in the current model have a spherical shape. If irregular shaped particles are employed, they
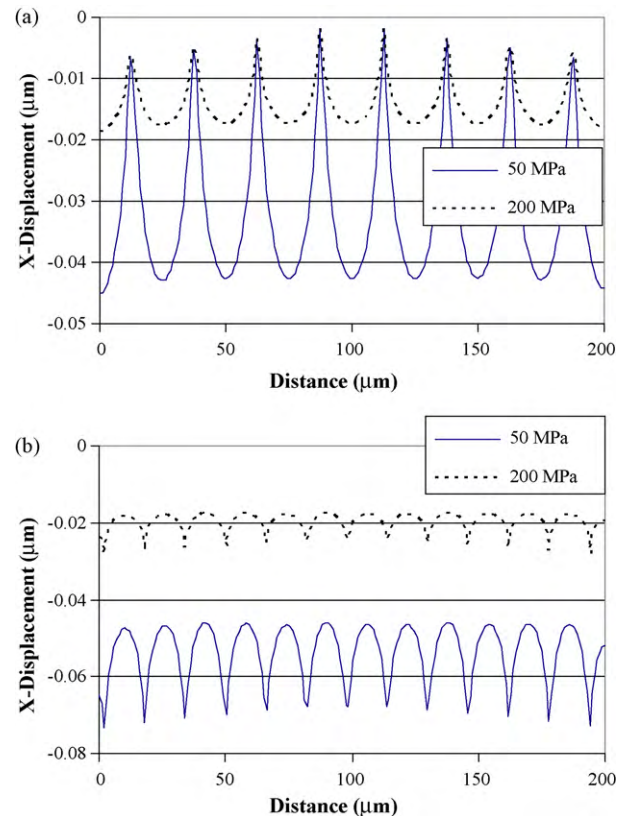

Fig. 7. The indentations into the separator made by (a) negative particles and (b) positive particles at $t = 0$ s under a pressure of 10 psi. Simulations were performed with two levels of Young's modulus for the separator, $E = 50$ and 200 MPa.
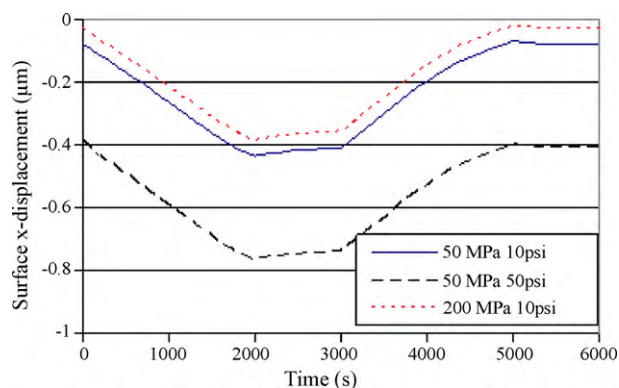
Fig. 8. The displacement-history plots at the right hand end of the cell, predicted by a half-sized 2D RVE. Three cases were investigated: a separator with a Young's modulus of $E = 50$ MPa under a pressure of $P = 10$ psi, under a pressure of $P = 50$ psi, and a separator with a Young's modulus of $E = 200$ MPa under a pressure of 10 psi.
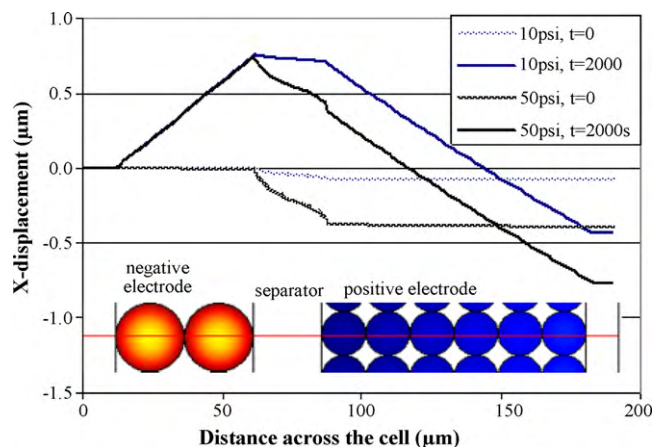

Fig. 9. The through thickness displacement at $t = 0$ and 2000 s (end of charge) predicted by a half-sized 2D RVE. The RVE had a separator with a Young's modulus of $E = 50$ psi under a pressures of 10 or 50 psi. The insert displays the Li concentration across the cell at $t = 2000$ s. The range of concentration in particles in the negative electrode is $(1.2–1.6) \times 10^4$ mol m^{-3} (SOC = 0.45–0.61). The range of concentration in particles in the positive electrode is $(5.5–7.2) \times 10^3$ mol m^{-3} (SOC = 0.24–0.31).

may be pressed into the separator. Similar situations are when an irregular shaped foreign particle is landed at the surface of the separator during manufacturing or a dendrite forms at a particle surface near the separator. In these cases, a non-slipping interface may be created and a local tensile stress may arise.

The variation of the cell thickness during the charge–discharge cycle was measured by monitoring the x-displacement at the midpoint at the right hand end of the cell. Fig. 8 presents the predicted displacement–time history at this point during the charge–discharge cycle for three different conditions: a separator of $E = 50$ MPa under $P = 10$ psi, under $P = 50$ psi, and a separator of $E = 200$ MPa under a pressure of 10 psi. For the simulated cases, the thickness change of the cell was always negative and its value varied with the charge–discharge cycle. The maximum reduction happened at 2000 s. The value was about -0.4 μm for a pressure of 10 psi and -0.8 μm for a pressure of 50 psi, respectively.

The dimensional change in individual components was investigated by inspecting the displacement profiles. Fig. 8 compares the displacement profiles through the thickness of the cell at $t = 0$ and 2000 s for a RVE with a separator of $E = 50$ MPa under two pressures. The displacement profile at $t = 0$ s clearly shows that the initial reduction in the cell thickness was related to the pressure and was mainly absorbed by the deformation of the separator. The profiles at other time intervals revealed a simultaneous deformation in the two electrodes. During the charging period, the thickness in the negative electrode increased while the thickness in the positive electrode reduced, as shown in the profile at $t = 2000$ s. The trend reversed during the discharging period. The thickness of the separator remained nearly constant during the cycle. The net change in the cell thickness was negative.

The average strain in each component can be estimated using the following relation:

$$\varepsilon^{ave} = \frac{\Delta l}{l} \tag{17}$$

where Δl is the displacement over a component of length l. Δl was measured across the cell thickness alone a line where the separator is in contact with electrode particles both side, as shown in the insert of Fig. 9. The computed average strains in the two electrodes, separator and the cell at $t = 2000$ s are summarized in Table 5. For the four cases investigated, the average strain is about 1.52% in the negative electrode and -1.12% in the positive electrode.

Assuming an isotropic volume expansion of ΔV, the linear expansion of an electrode for a given SOC range can be estimated using the following relationship:

$$\varepsilon = \text{SOC} \cdot (\Delta V)^{1/3} \tag{18}$$

The predicted through thickness strains for electrodes are compared with the linear expansion values estimated using Eq. (18) in Table 5. The values of the predicted through thickness strains are higher than the estimated linear strains. The additional strain in the FE model prediction is due to the non-isotropic expansion of the particles. In a close-packed pattern, the particles were unable to expand in-plane and the volume change was accommodated by deformation through the thickness at a higher rate.

The average strain in the separator varied with the elastic modulus of the separator and the pressure. The Δl measured along the line in Fig. 9 represents the average strain at its upper bound, according to the indentation profiles in Fig. 7. The average strain obtained by this way is about 35–120% higher when compared to the nominal strain estimated from the elastic relation:

$$\varepsilon_{nominal} = \frac{P}{E} \tag{19}$$

where P is the pressure and E is the elastic modulus of the separator.

The predicted maximum thickness variation for the RVE cell was about 0.2%. This value seems to be low as compared to the val-

Table 5
The change of SOC in the two electrodes and the resulted average strain (%) for a half-sized RVE cell and its components.

Case E(separator)/pressure	Negative electrode SOC 0.22–0.57	Positive electrode SOC 0.23–0.57	Separator	Separator (estimated) Eq. (19)	Cell total
50 MPa/10 psi	1.53	−1.12	−0.2	−0.14	−0.22
50 MPa/50 psi	1.52	−1.13	−1.2	−0.69	−0.39
200 MPa/10 psi	1.52	−1.12	−0.05	−0.035	−0.20
200 MPa/50 psi	1.51	−1.10	−0.38	−0.17	−0.20
Predicted average	1.52	−1.12			
Estimated for the SOC range (Eq. (18))	1.28	−0.954			

ues obtained in an experimental study on $LiC_6/LiPF_6/LiCoO_2$ battery [43]. The reported thickness variation was 7.69 μm when averaged for a cell using natural graphite and 2.29 μm for using mesophase carbon micro beads (MCMB). The cell thickness was 171 μm. This translates into a linear strain of 4.49 and 1.34% respectively.

It should be noted the thickness variation predicted by the current model is due to Li insertion/removal only. As mentioned in Section 3.4, the thermal expansion due to self-heating of the battery and the volume expansion due to gas generation in the Li-ion batteries [35] will also result in volume change. The volume variation due to Li insertion/removal and thermal expansion are cyclic whereas the volume expansion due to gas generation increases gradually over time. Our preliminary result showed that the volume expansion of the battery due to temperature rise as the result of heat generation alone is greater than that due to Li insertion [25].

The smaller dimensional change of the battery cell in the present study can also be partially attributed to a better cell design. The maximum expansion of $LiCoO_2$ positive electrode is in the range of 1% [43] whereas the maximum volume change of $Li_yMn_2O_4$ positive electrode is 6.5%. Because the volume variation of the two electrodes is opposite in sign, it is the difference in volume change between the two electrodes, instead of the absolute expansion of one electrode, determines the volume variation of the battery cell. From this perspective, a $LiC_6/Li_yMn_2O_4$ battery would have a smaller net volume variation as compared to a $LiC_6/LiCoO_2$ battery. Furthermore, in the present battery model, the thickness of the positive electrode was about twice of the value of the negative electrode. On the other hand, the volume expansion of the positive electrode was about a half of the negative electrode. This combination further reduced the difference in volume change between the two electrodes and thus produced a cell with a very small net dimensional change. The result suggests that the dimensional change of the battery may be reduced by optimizing the thickness ratio of the two electrodes in accordance with their volume expansion ratio.

5.3. Stress analysis

The stress state and its magnitude were found to vary greatly across the RVE cell in both temporal and spatial senses. As an example, Fig. 10 presents the x-stress and x-strain profiles at t = 2000 s across the thickness of the RVE along the line in the insert in Fig. 9. As seen, there are periodical hills and valleys in the profiles corresponding to the periodical location of the particles. At 2000 s, the charge had just stopped, a Li concentration gradient still existed in the particles. For the negative particles, the surface Li concentration was higher than the center. This resulted in a strain gradient in the particle. The stress gradient was opposite in sign with the
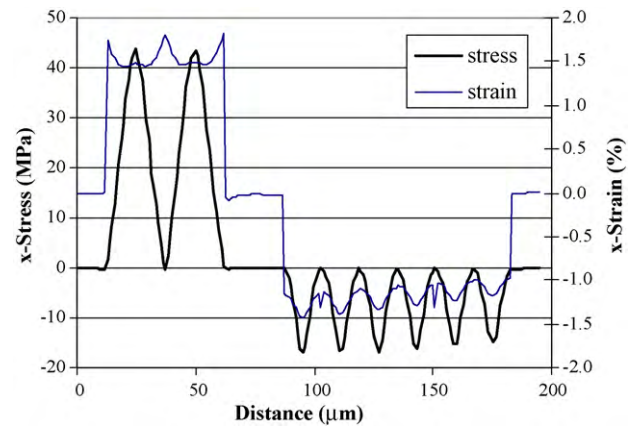

Fig. 10. The x-stress and x-strain distribution across a half-sized 2D RVE at t = 2000 s. The RVE had a separator with a Young's modulus of E = 200 MPa under a pressure of 10 psi. The range of SOC: SOC = 0.45–0.61 in the negative electrode, and SOC = 0.24–0.31 in the positive electrode.

strain gradient. A maximum tensile intercalation stress of 43 MPa was found at the center of the negative particles. The trend was opposite in the positive particles. The center of the positive particle had a higher Li concentration than its surface and the intercalation stress was therefore compressive.

The normal stress components in the separator were found predominantly compressive. As an example, Fig. 11 presents the distributions of the normal stresses and the shear stress in the separator at t = 5000 s for E = 50 MPa under a pressure of 10 psi. High compressive stresses can be seen in the area in contact with the particles. The stress was higher at the side with larger diameter of particles.

The variation of the stress during the charge and discharge cycles at a location of high stress near a negative particle was inspected. Fig. 12 presents a summary of stress history plots for the normal stresses and the Von Mises stress. The four rows correspond to four different cases. The first three rows are for a cell under a pressure of 10 psi. The separator had a Young's modulus of E = 50 MPa, E = 200 MPa and E = 2000 MPa, respectively. The fourth row is for E = 2000 MPa under a pressure of 50 psi. As shown, the two normal stresses were compressive when the Young's modulus of the separator is low. Increasing the Young's modulus of the separator moved the curve up, i.e. towards the tensile direction. For the case of a separator of E = 2000 MPa under 10 psi, the normal stress components became tensile. Nevertheless, increasing the pressure to 50 psi was sufficient to suppress the tensile stress in the separator, as shown in the fourth row. The result indicates that increasing surface pressure
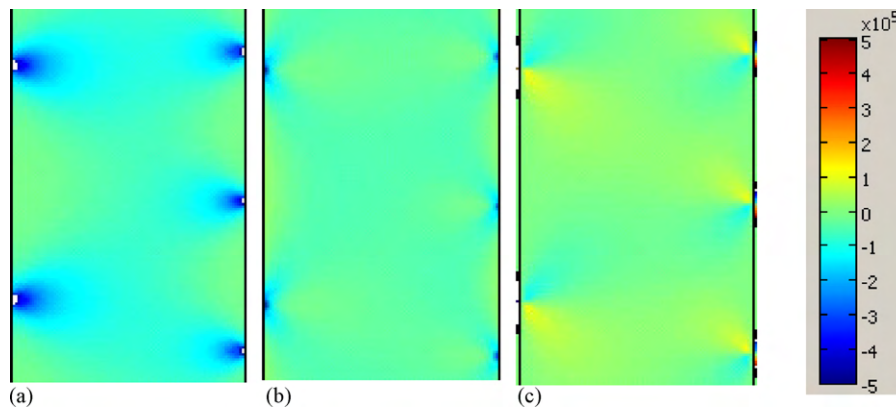

Fig. 11. (a) σ_x, (b) σ_y and (c) τ_{xy} stress components in the separator in a cell with regularly close-packed particles, at t = 5000 (the end of discharge). The displayed case is for a half-sized 2D RVE with separator with a Young's modulus of E = 50 MPa under a pressure of 10 psi.
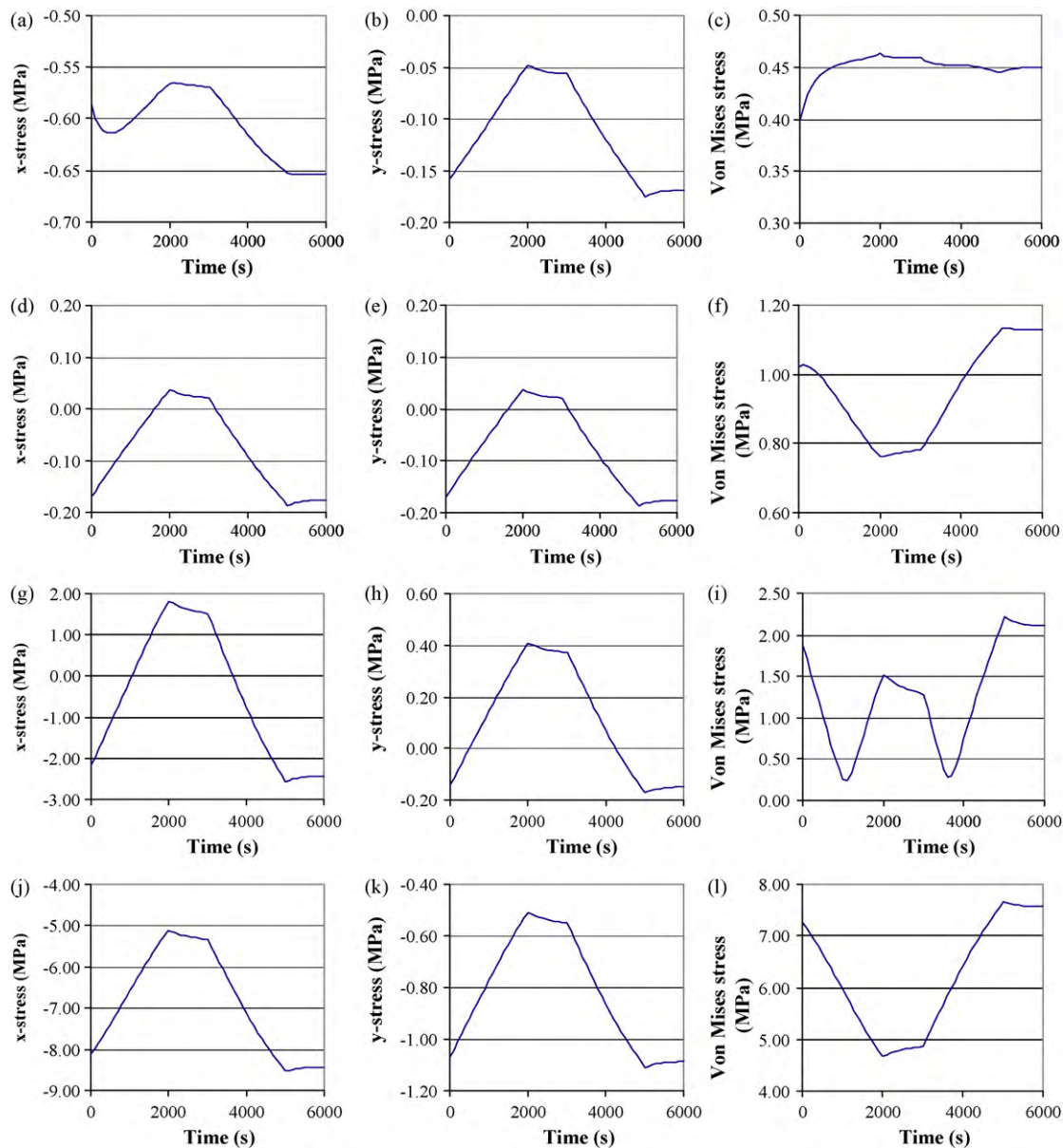
Fig. 12. The history plots of the normal stress components (x and y) and the Von Mises stress in the separator near a negative particle. (a–c) In a separator with a Young's modulus of $E = 50$ MPa under a pressure of $P = 10$ psi; (d–f) in a separator of $E = 200$ MPa under $P = 10$ psi; (g–i) in a separator of $E = 2000$ MPa under $P = 10$ psi; (j–l) in a separator of $E = 2000$ MPa under $P = 50$ psi. The stress components were predominately compressive when the separator had a low elastic modulus or the cell was subjected to a pressure that was sufficiently high.

would help to prevent separator failure by suppressing the tensile stress. It should be noted that, because of the limitation on contact modeling in the current model, the results reported here are only qualitative indications.

5.4. Viscoelastic relaxation

Because a polymeric separator is considered in this work, the viscoelastic relaxation of the separator cannot be neglected. To examine this effect, a hypothetical viscoelastic material described by a simple linear viscoelastic material law was assumed such that

$$G = G_0 + \sum_i G_i \, e^{-t/\tau_i} \qquad (20)$$

where G is shear modulus, G_0 is the instantaneous and G_i is the time-dependent components of the shear modulus, respectively, and τ_i is the characteristic relaxation time. For a direct comparison, an

elastic material model was constructed with a shear modulus being equal to the summation of the instantaneous and time-dependent moduli in the viscoelastic law. Table 6 provides a summary of the assumed material laws and their parameters. Fig. 13 compares the history plots of the normal stress components and the Von Mises stress in the separator predicted using these two material laws. The result shows that stress relaxation modified the shape of the stress history curves and reduced the amplitude of the cyclic stress. This

Table 6
Hypothetic viscoelastic parameters for the separator.

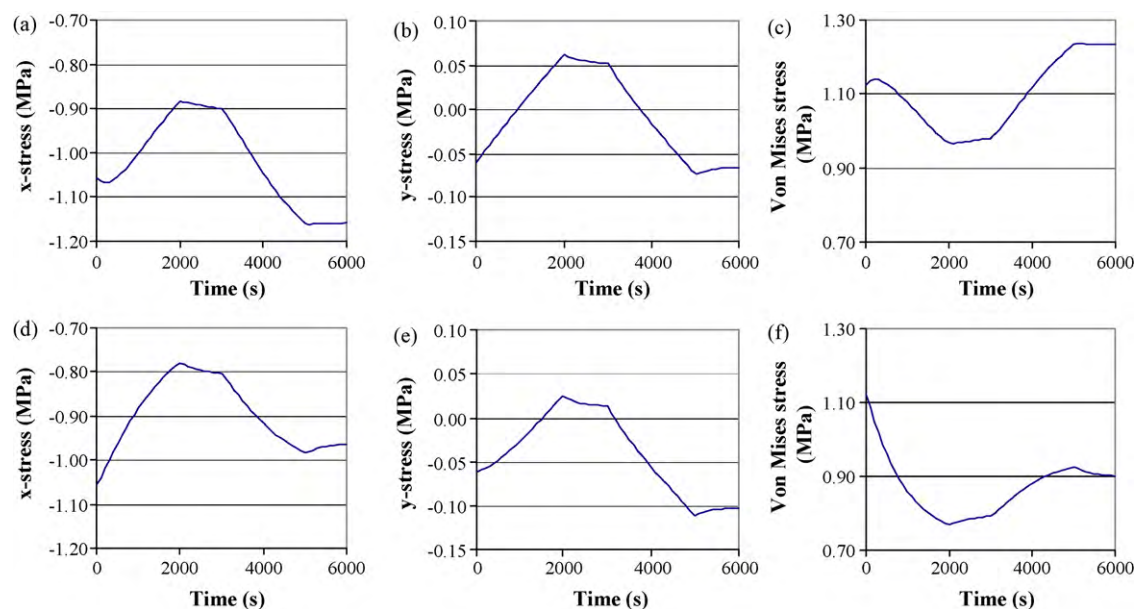| i	Elastic $G = G_0$	Viscoelastic $G = \sum G_i \, e^{-t/\tau_i}$	
		G_i (MPa)	τ_i (s)
0	85	50	–
1		35	500

Fig. 13. The history plots of the normal stress components (x and y) and the Von Mises stress in the separator near a negative particle. (a–c) In a separator with a shear modulus of $G_0 = 85$ MPa; (d–f) in a separator with an assumed viscoelastic property given in Table 6. The cell was subjected to a pressure of 10 psi.

effect is expected to increase when the self-heating of the battery is considered in the analysis.

It should be noted that the simulation result presented here should be treated as qualitative rather than quantitative at this stage. The investigations with the 2D RVE sub-models were based on estimated material parameters and simple material laws. The interface between the separator and particles was modeled with a continuous mesh instead of a contact definition. Nevertheless, a non-slipping interface may be created when irregular shaped particles, such as a foreign particle or dendrite, are present at the surface of the separator. In this case, the results of a continuous mesh would be more relevant.

6. Summary and conclusions

A multi-scale modeling approach for the stress analysis of a basic Li-ion battery cell was proposed. In this approach, the multi-physics equations were solved concurrently using three sub-models at three different scales. The battery electrochemical kinetics and the coupling between diffusion and battery kinetics were solved by a 1D macroscopic battery sub-model and a microscopic sub-model for spherical particles based on an existing Li-ion battery model in COMSOL®. The stress analysis at the level of a battery cell was conducted with a meso-scale representative volume element (RVE) sub-model of the battery cell. Based on this approach, a multi-scale model with the inclusion of intercalation stress was developed for a $LiC_6/LiPF_6/Li_yMn_2O_4$ battery cell.

Numerical investigations were carried out with 2D RVE sub-models. Simulation results provided new insights into the deformation of battery components caused by Li insertion/removal in a charge and discharge cycle. It was observed that the net cyclic dimensional variation of the battery cell was determined by the difference of the volume change of the two electrodes and this amount may be regulated by optimizing the thickness ratio of the two electrodes in accordance with their volume expansion ratio. For the $LiC_6/LiPF_6/Li_yMn_2O_4$ battery cell analyzed, the maximum thickness variation caused by Li insertion/removal was about 0.2% under a pressure of 10 psi.

Under pressure, the electrode particles made small indention into the separators. The local strain at the indented areas was much higher than the nominal strain of the separator. The maximum stress in the separator was found in indented areas. The stress state and its magnitude in the separator depended upon the particle size, particle packing, and the boundary constraint of the battery cell. Particles with a loose-packed pattern showed the tendency to result in tensile stresses in the separator. With a close-packed particle pattern, under a sufficient pressure, the normal stresses in the separator were predominately compressive. Due to the limitation in modeling contact in the current model, the above results should be treated as qualitative indications only.

Considering viscoelastic relaxation in the analysis resulted in a modified stress response. For a polymeric membrane separator, to have a reasonable estimation of the stress in separator, the viscoelastic relaxation of the separator material and the thermal stress need to be included in the analysis.

References

[1] S.S. Zhang, Journal of Power Sources 164 (2007) 351–364.
[2] P. Arora, Z.M. Zhang, Chemical Reviews 104 (2004) 4419–4462.
[3] R. Baldwin, NASA/TM-2009-215590, 2009.
[4] M.D. Farrington, Journal of Power Sources 80 (1999) 278–285.
[5] M.D. Farrington, Journal of Power Sources 96 (2001) 260–265.
[6] Y.T. Cheng, M.W. Verbrugge, Journal of Applied Physics 104 (2008).
[7] J. Christensen, J. Newman, Journal of Solid State Electrochemistry 10 (2006) 293–319.
[8] J. Christensen, J. Newman, Journal of the Electrochemical Society 153 (2006) A1019–A1030.
[9] X.C. Zhang, W. Shyy, A.M. Sastry, Journal of the Electrochemical Society 154 (2007) A910–A916.
[10] K.E. Aifantis, J.P. Dempsey, Journal of Power Sources 143 (2005) 203–211.
[11] Y.T. Cheng, M.W. Verbrugge, Journal of Power Sources 190 (2009) 453–460.
[12] R.E. Garcia, Y.M. Chiang, W.C. Carter, P. Limthongkul, C.M. Bishop, Journal of the Electrochemical Society 152 (2005) A255–A263.

[13] D. Bernardi, E. Pawlikowski, J. Newman, Journal of the Electrochemical Society 132 (1985) 5–12.
[14] T. Ohshima, M. Nakayama, K. Fukuda, T. Araki, K. Onda, Electrical Engineering in Japan 157 (2006) 17–25.
[15] L. Rao, J. Newman, Journal of the Electrochemical Society 144 (1997) 2697–2704.
[16] K.E. Thomas, J. Newman, Journal of the Electrochemical Society 150 (2003) A176–A192.
[17] X.C. Zhang, A.M. Sastry, W. Shyy, Journal of the Electrochemical Society 155 (2008) A542–A552.
[18] S.C. Chen, C.C. Wan, Y.Y. Wang, Journal of Power Sources 140 (2005) 111–124.
[19] Y. Chen, J.W. Evans, Journal of the Electrochemical Society 140 (1993) 1833–1838.
[20] Y.F. Chen, J.W. Evans, Electrochimica Acta 39 (1994) 517–526.
[21] Y.F. Chen, J.W. Evans, Journal of the Electrochemical Society 143 (1996) 2708–2712.
[22] C.R. Pals, J. Newman, Journal of the Electrochemical Society 142 (1995) 3274–3281.
[23] C.R. Pals, J. Newman, Journal of the Electrochemical Society 142 (1995) 3282–3288.
[24] COMSOL, 3.5, 2009.
[25] W. Wu, X. Xiao, D. Shi, ASME World Congress, Vancouver, 2010.
[26] S. Golmon, K. Maute, M.L. Dunn, Computers & Structures 87 (2009) 1567–1579.
[27] M. Doyle, T.F. Fuller, J. Newman, Journal of the Electrochemical Society 140 (1993) 1526–1533.
[28] M. Doyle, J. Newman, A.S. Gozdz, C.N. Schmutz, J.M. Tarascon, Journal of the Electrochemical Society 143 (1996) 1890–1903.
[29] Y. Benveniste, Mechanics of Materials 6 (1987) 147–157.
[30] T. Mori, K. Tanaka, Acta Metallurgica 21 (1973) 571–574.
[31] M.W. Verbrugge, Y.T. Cheng, Journal of the Electrochemical Society 156 (2009) A927–A937.
[32] C.W. Wang, A.M. Sastry, Journal of the Electrochemical Society 154 (2007) A1035–A1047.
[33] T. Kanit, S. Forest, I. Galliet, V. Mounoury, D. Jeulin, International Journal of Solids and Structures 40 (2003) 3647–3679.
[34] F.P. Beer, J.E.R. Johnston, J.T. Dewolf, D.F. Mazurek, Mechanics of Materials, 5th ed., McGrow-Hill, New York, 2009.
[35] J.-S. Shin, C.-H. Han, U.-H. Jung, S.-I. Lee, H.-J. Kim, K. Kim, Journal of Power Sources 109 (2002) 47–52.
[36] S. Prussin, Journal of the Electrochemical Society 108 (1961) C213–C1213.
[37] Y. Qi, H. Guo, L.G.J. Hector, A. Timmons, J Electrochemical Society 157 (2010) A558–566.
[38] W. Wu, X. Xiao, submitted for publication.
[39] K.R. Kganyago, P.E. Ngoepe, Physical Review B 68 (2003).
[40] http://www.cevp.co.uk/general_graphite.htm, 2009.
[41] R.P. Ramasamy, J.W. Lee, B.N. Popov, Journal of Power Sources 166 (2007) 266–272.
[42] H.J. Peng, X. Qin, L. Xiong, C. Jing Fang, Journal of Acta Mechanica Sinica 25 (2009) 565–570.
[43] M. Majima, T. Tada, S. Ujiie, E. Yagasaki, S. Inazawa, K. Miyazaki, Journal of Power Sources 81 (1999) 877–881.